ZNF296 Drives Immune Evasion in Epithelial Cancers by Repressing Immune Stimulatory Genes

Hefei Wang[1,2], Fangting Zhao[1], Yao Li[1], Peiyu Wang[3], Yixue Wang[1], Pengfei Ren[3], Changhe Li[1], Hanqiu Zheng[1], Zexian Zeng[2,3], and Deng Pan[1,2]

ABSTRACT

Resistance to immune-mediated destruction is a fundamental hallmark of cancer. Although several mechanisms have been identified that facilitate immune evasion, the transcriptional programs that orchestrate this process remain poorly understood. In this study, through a genome-wide CRISPR activation screen in human cancer cells subjected to NK cell–mediated killing, we identified ZNF296, a transcription factor highly expressed in epithelial cancers, as a key driver of tumor resistance to both NK and cytotoxic T-cell–mediated immunity. In mouse models, inhibition of ZNF296 significantly enhanced both NK and T-cell–mediated antitumor immunity, leading to a marked reduction in metastasis and increased infiltration of immune cells into the tumor microenvironment. Mechanistically, ZNF296 induced strong transcriptional repression of IFN-stimulated genes and key immunostimulatory ligands critical for NK and T-cell–mediated cytotoxicity. At the molecular level, ZNF296 directly interacted with and recruited the NuRD chromatin remodeling and deacetylase complex to the promoters of its target genes to suppress expression. Notably, treatment with low-dose romidepsin, an FDA-approved inhibitor targeting histone deacetylase 1, a core component of the NuRD complex, effectively restored NK and T-cell–mediated killing in cancer cells with high ZNF296 expression. Collectively, these findings establish ZNF296 as a key regulator of immune evasion, driving resistance to both NK and T-cell–mediated antitumor immunity, and highlight its potential as a therapeutic target to overcome immune resistance in epithelial cancers.

Significance: ZNF296 is a transcriptional regulator that enables cancer cells to evade immune surveillance, offering possibilities for developing treatments that enhance the ability of the immune system to eliminate cancer cells.

Introduction

Tumor immune evasion is the fundamental driver of cancer progression and metastasis. Understanding the mechanisms that enable tumors to escape immune surveillance is critical for improving the efficacy of cancer immunotherapies. T and NK cells are essential components of immune surveillance, acting as first-line defenders by directly killing tumor cells and coordinating broader immune responses (1, 2). The identification of tumor-intrinsic resistance mechanisms that undermine these immune cells is a crucial area of research in the field of cancer immunology. Recent advances, including CRISPR-based genetic screens, have provided significant insights into the molecular pathways by which tumors evade immune responses mediated by both NK and T cells. For instance, using genome-wide CRISPR screens, we and others have identified many tumor-intrinsic resistance mechanisms that drive escape to T-cell–mediated killing (3–12). Complementary studies have used NK cell coculture systems to elucidate the mechanisms underlying tumor resistance to NK cell–mediated killing. These efforts have identified the downregulation of NK cell activation ligands, such as B7-H6, and the upregulation of inhibitory ligands, including HLA-E, as pivotal contributors to immune escape (5, 6, 13, 14). Moreover, CHMP2A, identified via CRISPR screening, promotes NK resistance by enhancing extracellular vesicle secretion of MICA/B and TRAIL, which suppress NK cell function (7). Together, these findings highlight the diverse and complex strategies employed by tumors to evade immune responses and underscore the importance of further exploring these pathways to develop novel therapeutic strategies.

Tumors undergo dynamic transcriptional alterations during cancer progression, which plays a pivotal role in immune evasion. Transcription factors (TF), which are key regulators of gene expression, orchestrate tumor immune escape by modulating specific transcriptional programs. For instance, the TF FOXA1 suppresses the activity of STAT2, leading to the downregulation of IFN response genes and subsequent immune evasion (15). Interestingly, the epithelial-to-mesenchymal transition (EMT) transcriptional state is closely associated with sensitivity to NK-mediated killing. Tumors with epithelial-like traits are often resistant to NK cell–mediated cytotoxicity (5, 16). These studies underscore the critical role of transcriptional programs in determining tumor sensitivity to immune-mediated killing.

ZNF296 is a zinc-finger protein that plays a crucial role in embryonic development and epigenetic regulation. In embryonic stem cells, it is essential for maintaining a global epigenetic state, reducing chromatin accessibility, and repressing H3K9 methylation (17–19). Recent studies have also implicated ZNF296 in tumor

[1]School of Basic Medical Sciences, State Key Laboratory of Molecular Oncology, Tsinghua University, Beijing, China. [2]Tsinghua-Peking Joint Centre for Life Sciences (CLS), Beijing, China. [3]Center for Quantitative Biology, Academy for Advanced Interdisciplinary Studies, Peking University, Beijing, China.

H. Wang and F. Zhao contributed equally to this article.

Current address for Y. Li: Department of Microbiology, Harvard Medical School, Boston, Massachusetts; Department of Cancer Immunology and Virology, Dana-Farber Cancer Institute, Boston, Massachusetts.

Corresponding Authors: Deng Pan, School of Basic Medical Sciences, Tsinghua University. Medical Science Building B1005, Tsinghua University, Beijing 100084, China. E-mail: dpan@tsinghua.edu.cn; and Zexian Zeng, Center for Quantitative Biology, Academy for Advanced Interdisciplinary Studies, Peking University, Lu-Zhihe Building 235, Peking University, Beijing 100084, China. E-mail: zexianzeng@pku.edu.cn

Cancer Res 2026;86:116–30

doi: 10.1158/0008-5472.CAN-25-0153

progression. ZNF296 is overexpressed in acute myeloid leukemia and acute lymphoid leukemia (20), and its expression is upregulated in tumor regions in a mouse model of colon carcinogenesis (21). Although these studies suggest a correlation between ectopic ZNF296 expression and tumor progression, the precise functional roles and mechanistic pathways through which ZNF296 contributes to cancer development remain unclear. In this study, we identified that tumor-intrinsic ZNF296 plays a key role in regulating antitumor immunity.

Materials and Methods

Cell culture

A549 cells (RRID: CVCL_0023) and MDA-MB-453 cells (RRID: CVCL_0418) were obtained from the Chinese National Collection of Authenticated Cell Cultures. CAMA1 cells (RRID: CVCL_1115) were obtained from Meisen Chinese Tissue Culture Collection. MC38 cells (RRID: CVCL_B288) were obtained from Biofeng. B16F10 cells were kindly provided by Prof. Haidong Tang (Tsinghua University, Beijing, China), and 4T1 cells were kindly provided by Prof. Chaoxia Zou (Harbin Medical University, Harbin, China). Cell lines were authenticated by short tandem repeat profiling and routinely tested for *Mycoplasma* contamination using a PCR-based method (*Mycoplasma* detection protocol from the Broad Institute). All experiments used cells within short passages from original stocks.

A549 cells (RRID: CVCL_0023), CAMA1 cells (RRID: CVCL_1115), B16F10 cells (RRID: CVCL_XH27), and MC38 cells (RRID: CVCL_B288) were cultured in DMEM supplemented with 10% FBS and 1% penicillin–streptomycin (PenStrep). MDA-MB-453 cells (RRID: CVCL_0418) and 4T1 cells (RRID: CVCL_0125) were maintained in RPMI-1640 medium supplemented with 10% FBS and 1% PenStrep. NK-92-MI cells were cultured in α-minimum essential medium without ribonucleosides (Thermo Fisher Scientific), supplemented with 0.2 mmol/L Myo-inositol (Sigma-Aldrich), 0.1 mmol/L 2-mercaptoethanol (Gibco), 0.02 mmol/L folic acid (Sigma-Aldrich), 12.5% FBS, and 12.5% horse serum.

Genome-scale CRISPR-dCas9 tumor cell and NK cell coculture screen in A549 cells

A549 cells were transduced with the lentiviral vector, dCas9-VP64_Blast (Addgene, #61425, RRID: Addgene_61425), to generate dCas9-VP64–expressing cells. A549-dCas9-VP64 cells were then transfected with the Calabrese P65-HSF pooled library (Addgene, #1000000111, RRID: Addgene_1000000111) at an infection rate of approximately 10% to control the single-guide RNA (sgRNA) infection rate. After 48 hours, the transduced cells were selected using puromycin (InvivoGen, cat. #ant-pr-1). After 10 days of selection, the cells were divided into control and experimental groups with three replicates per group. Each replicate contained 4×10^7 cells and maintained 500× sgRNA coverage. The experimental groups were cocultured with NK-92MI cells at a 1:1 effector-to-target (E:T) ratio, whereas the control group was cultured with NK-92MI cell medium alone. After 24 hours of coculture, NK-92MI cells were removed, and the tumor cells were washed with PBS to eliminate both NK-92MI cells and dead tumor cells. Tumor cells were harvested using trypsin, and genomic DNA was extracted using the NucleoSpin Blood XL kit. PCR was performed to selectively amplify the sgRNA region, followed by Illumina sequencing to determine the sgRNA abundance. CRISPR screen data were processed and analyzed using MAGeCK (version 4.1.3; ref. 22). FASTQ reads from the CRISPR screen were processed using a count module. The robust rank aggregation (RRA) module (default setting) was used to calculate the $\log_2$ fold changes (LFC) and *P* values of the genes. Customized R scripts were used to visualize the data.

ZNF296 overexpression using a CRISPR activation system

The sgRNA sequences used to generate ZNF296 overexpression cell lines are listed in Supplementary Table S1. The ZNF296 sgRNA was cloned into the pXPR_502 plasmid (Addgene, #96923, RRID: Addgene_96923) and confirmed by Sanger sequencing. sgRNA constructs were cotransfected with psPAX2 (Addgene, #12260, RRID: Addgene_12260) and pMD2.G (Addgene, #12259, RRID: Addgene_12259) and mixed with 1:4 polyethyleneimine (PEI) in Opti-MEM for lentivirus production. The virus was harvested 48 hours after transfection and used to infect the A549 cells. Puromycin (6 μg/mL) was added to the culture to select for sgRNA-transduced cell lines.

ZNF296 overexpression using lentiviral expression vectors

Lentiviral vectors encoding human ZNF296 (ENSG00000170684) were generated by amplifying Gibson assembly cloning–compatible inserts from cDNA derived from A549 cells. The PCR-amplified products were purified and cloned into pHAGE-PGK-3×flag-EGFP and pCMV-puro vectors using the Seamless Assembly cloning kit (CloneSmarter, cat. #C5891), according to the manufacturer's instructions. Successful cloning was confirmed by Sanger sequencing. For lentivirus production, ZNF296-expressing lentiviral vectors and an empty vector control were cotransfected with psPAX2 (Addgene, #12260; RRID: Addgene_12260) and pMD2.G (Addgene, #12259; RRID: Addgene_12259) using a 1:4 PEI ratio in Opti-MEM. After 48 hours of transfection, the lentiviral particles were harvested and used to infect A549 cells. Following infection, cells overexpressing ZNF296 were either sorted for GFP^+ cells using FACS (for pHAGE-PGK-3× Flag-EGFP) or selected using puromycin (6 μg/mL) for cells transfected with the pCMV-puro vector.

ZNF296 knockdown using a CRISPR interference system

The sgRNA sequences used to generate the ZNF296/Zfp296 knockdown (KD) cell lines are listed in Supplementary Table S2. ZNF296/Zfp296 sgRNA was cloned into the lenti-EF1a-dCas9-KRAB-puro plasmid (a gift from the Mo Chen Lab, Tsinghua University). Successful cloning was confirmed by Sanger sequencing. For lentivirus production, sgRNA constructs were cotransfected with psPAX2 (Addgene, #12260) and pMD2.G (Addgene, #12259) using a 1:4 PEI ratio in Opti-MEM. The lentivirus was harvested 48 hours after transfection and used to infect MDA-MB-453 (for ZNF296 KD) and 4T1 cells (for Zfp296 KD). Following infection, puromycin (6 μg/mL) was added to the culture to select sgRNA-transduced cell lines.

Histone deacetylase 1 KD using a short hairpin RNA system

To inhibit histone deacetylase 1 (HDAC1), specific short hairpin RNA (shRNA) sequences used to target each gene are listed (Supplementary Table S3). The shRNA was cloned into the pLKO.1-puro plasmid (purchased from YouBio, cat. #VT1792). The constructs were validated by Sanger sequencing. Lentiviral particles for each shRNA construct were produced by cotransfecting shRNA-expressing plasmids with psPAX2 (Addgene, #12260) and pMD2.G (Addgene, #12259) into HEK293T cells (RRID: CVCL_0063) using a 1:4 PEI ratio in Opti-MEM. The lentivirus was harvested 48 hours after transfection and used to infect the A549 cells. Following infection, puromycin

(6 μg/mL) was added to the culture medium to select shRNA-transduced cells.

Isolation and expansion of human primary NK and T cells

Peripheral blood mononuclear cells of healthy donors were purchased from Milestone Biotechnologies with written informed consent and approved by the Shanghai Liquan Hospital Institutional Review Board. The studies were conducted in accordance with the Declaration of Helsinki.

Peripheral blood mononuclear cells were recovered by cryopreservation, and NK cells were sorted using the Human NK Cell Isolation Kit (Miltenyi Biotec, cat. #130-092-657). The isolated NK cells were then activated using the Human NK Cell Activation/Expansion Kit (Miltenyi Biotec, cat. #130-094-483), which employs anti-CD2 and -CD335 antibodies. Peripheral blood NK cells were cultured in X-VIVO 15 medium (Lonza) supplemented with 1% heat-inactivated human serum AB (GeminiBio, cat. #100-512), 1% PenStrep, and 50 IU/mL human IL2. Fresh human IL2 was added every 3 days or with each medium change.

EasySep Human $CD8^+$ T Cell Isolation Kit (STEMCELL Technologies, cat. #19053) was used for T-cell isolation. The isolated $CD8^+$ T cells were then activated using anti–human CD3 (BioLegend, cat. #317326; RRID: AB_11150592) and anti–human CD28 (BD Biosciences, cat. #555725; RRID: AB_396068) antibodies for 24 hours. CD8 T cells were cultured and expanded in X-VIVO 15 medium (Lonza, cat. #02-060Q) supplemented with 10% heat-inactivated FBS and 20 ng/mL recombinant human IL2 (BioLegend, cat. #575408). The 1G4 T-cell receptor (TCR) was transduced into $CD8^+$ T cells after 1 day of activation. The 1G4 TCR-positive T cells were then sorted for further experiments.

Isolation and expansion of mouse primary NK cells

The mice were sacrificed, and their spleens were harvested for NK cell isolation. The spleens were dissociated into single-cell suspensions. NK cells were isolated using a MojoSort Mouse NK Cell Isolation Kit (BioLegend, cat. #480050). Purified NK cells were cultured in RPMI medium supplemented with 10% FBS, PenStrep, GlutaMAX, β-mercaptoethanol, and nonessential amino acids. The culture was further supplemented with 40 ng/mL of recombinant mouse IL2 and 10 ng/mL of recombinant mouse IL15 to promote NK cell expansion.

Tumor cell and NK cell coculture experiments

We seeded 5×10^4 or 1×10^5 tumor cells into each well of a 24-well plate. NK-92MI or primary human/mouse NK cells were added at the indicated E:T ratios. In the control group, tumor cells were cultured in NK cell medium only. After 24 hours of coculture, NK cells were removed, and the tumor cells were harvested. Cells were stained with CD45-allophycocyanin (APC) and 4′,6-diamidino-2-phenylindole (DAPI) to identify NK cells and dead tumor cells, respectively. The number of viable tumor cells was then analyzed using flow cytometry, and the survival ratio was calculated using the formula: (viable tumor cells after coculture/viable tumor cells in control medium) × 100%.

Tumor cell and T-cell coculture experiments

We seeded 5×10^4 or 1×10^5 tumor cells into each well of a 24-well plate. For mouse T-cell coculture assays, tumor cells were pulsed with 100 ng/mL SIINFEKL peptide (GenScript, cat. #RP10611) for 2 hours in an incubator. For the human T-cell coculture assay, activated 1G4 TCR T cells were added at the indicated E:T ratios. For the mouse assay, activated OT-I $CD8^+$ T cells were added at the indicated E:T ratios. In the control group, tumor cells were cultured in T-cell medium only. After 24 hours of coculture, T cells were removed, and the tumor cells were harvested. Cells were stained with CD45-APC and DAPI to identify T cells and dead tumor cells, respectively. The number of viable tumor cells was then analyzed using flow cytometry, and the survival ratio was calculated using the formula: (viable tumor cells after coculture/viable tumor cells in control medium) × 100%.

RNA sequencing and analysis

Total mRNA from A549 and 4T1 cells was extracted using TRIzol (Invitrogen, cat. #15596026) and sequenced using Illumina protocols on HiSeq 2500. RNA sequencing (RNA-seq) reads were aligned to mm9 or GRCh38 genome using HISAT2 (version 2.2.1; RRID: SCR_015530; ref. 23) with default parameters. All the unmapped reads were removed. Read counts were calculated using featureCounts (version 2.0.6; RRID: SCR_012919; ref. 24) with uniquely mapped reads, differentially expressed genes identified using DESeq2 (version 1.44.0; RRID: SCR_000154; ref. 25), and the results visualized using ggplot2 (version 3.5.1; RRID: SCR_014601; ref. 26) and pheatmap (version 1.0.12; RRID: SCR_016418).

Enrichment analysis

Gene Ontology analysis for screen top hits

To identify significant pathways enriched or depleted in the screen, hypergeometric distribution statistics were applied to the top positively or negatively selected genes ($|LFC| > 2$ and $FDR < 0.05$). Gene Ontology (GO) analysis for molecular function was conducted using clusterProfiler (version 4.12.0; RRID: SCR_016884; ref. 27), and the results were visualized using ggplot2 (version 3.5.1; RRID: SCR_014601; ref. 26).

Gene set enrichment analysis for differential expressed genes from RNA-seq

To identify significant pathways affected by ZNF296, differentially expressed genes (A549: $|LFC| > 2$ and $FDR < 0.05$; 4T1: $|LFC| > 1$ and $FDR < 0.05$) from RNA-seq were used for gene set enrichment analysis (GSEA). GSEA was performed using clusterProfiler (version 4.12.0; ref. 27), and the results were visualized using ggplot2 (version 3.5.1; ref. 26).

GO analysis for ZNF296 interaction proteins

To identify complexes interacting with ZNF296, proteins interacting with ZNF296 were identified using immunoprecipitation (IP)–mass spectrometry. The results were analyzed for cellular components using clusterProfiler (version 4.12.0; ref. 27), and visualizations were generated using ggplot2 (version 3.5.1; ref. 26).

qRT-PCR

Total RNA was purified using TRIzol reagent (Invitrogen, cat. #15596018) according to the manufacturer's protocol. Extracted RNA (1 μg) was transcribed into cDNA using the HiScript III 1st Strand cDNA Synthesis Kit (Vazyme, cat. #R312-01) according to the manufacturer's protocol. The cDNA samples were diluted and used for qRT-PCR). Taq Pro Universal SYBR qPCR Master Mix (Vazyme, cat. #Q712-02) and gene-specific primers were used for PCR amplification and detection using LightCycler 480 (Roche). Differences in expression were calculated using the $2^{-\Delta\Delta C_t}$ method.

The primers (5′–3′) used for qPCR are listed in Supplementary Table S4.

Assay for transposase-accessible chromatin using sequencing and analysis

Three replicates of both the control and ZNF296-overexpressing (ZNF296-OE) samples were prepared. Assay for transposase-accessible chromatin using sequencing (ATAC-seq) was performed using 5×10^4 A549 cells using the Hyperactive ATAC-Seq Library Prep Kit for Illumina (Vazyme, cat. #TD711) and TruePrep Index Kit V2 for Illumina (Vazyme, cat. #TD202). The ATAC libraries were sequenced on an Illumina platform, and sequencing reads were aligned to the human genome (GRCh38/hg38) using Bowtie 2 (RRID: SCR_016368). MACS2 (version 2.2.7.1; RRID: SCR_013291; ref. 28) was used to call the peaks, and bigwigCompare (version 3.5.1; ref. 29) was applied to merge peaks from different samples into a consolidated peak set. Counts per million normalization were applied when generating BigWig files for both visualization and downstream analysis. Differentially bound regions were determined based on read counts using DiffBind (version 3.4.11; RRID: SCR_012918; ref. 30), defined by $|LFC| > 0.5$ and P value <0.05. HOMER (RRID: SCR_010881) was used for motif analysis, and peak annotations were assigned to gene loci using ChIPseeker (version 1.40.0; RRID: SCR_021322; ref. 31).

Flow cytometry for NK ligands

Tumor cells (5×10^5) were performed for flow cytometry staining. Each sample was stained with 1 μL of an antibody diluted in staining buffer (BioLegend, cat. #420201). The antibodies used for ligand staining were PE anti–human CD95 (Fas; BioLegend, cat. #305608; RRID: AB_314546), APC anti–human CD58 (BioLegend, cat. #330918; RRID: AB_2650886), and PE anti–human CD54 (BioLegend, cat. #353106; RRID: AB_10897647). DAPI was used to stain the dead cells.

Single-cell RNA-seq analysis

Single-cell RNA-seq (scRNA-seq) data (32) were obtained from the Gene Expression Omnibus (GEO; RRID: SCR_005012) public datasets (accession number: GSE176078). The original article contains seven subdatasets and is different by cell. Preprocessing, clustering, and annotation were performed on cancer epithelial cell subsets using the Scanpy tutorial code with the recommended parameters (https://scanpy.readthedocs.io/en/stable/tutorials/basics/clustering.html). Annotation of cell types was in accordance with the Leiden cluster and in-house marker sets. Gene expression was normalized to 10,000 for each cell, and the Vmax parameter was set to 100.

Chromatin IP sequencing and analysis

Cells (3×10^7) were cross-linked using 1% formaldehyde and quenched with 0.125 mol/L glycine. Lysates were prepared in a buffer (50 mmol/L HEPES-KOH pH 7.5, 1 mmol/L EDTA, 0.1% SDS, 140 mmol/L NaCl, 0.1% sodium deoxycholate, and 1% Triton X-100), sonicated on ice, and precleared. IP was performed overnight at 4°C using protein A/G Dynabeads (MedChemExpress, cat. #HY-K0202) coupled with the antibody complexes. Chromatin-immunoprecipitated DNA was purified after elution and reverse cross-linking, followed by library preparation and sequencing based on the established protocols. The antibodies used for chromatin IP (ChIP) included anti-FLAG (Sigma-Aldrich, cat. #F3165; RRID: AB_259529) for ZNF296 and anti-HDAC1 (Active Motif, cat. #40967; RRID: AB_2614948). Raw ChIP sequencing (ChIP-seq) reads were processed with trim_galore (version 0.6.7; RRID: SCR_011847) and aligned to the human genome (GRCh38/hg38) using Bowtie 2 (version 2.4.5; RRID: SCR_016368; ref. 33); the peaks were called with MACS2 (version 2.2.7.1; RRID: SCR_013291; ref. 28). Peaks were annotated using ChIPseeker (version 1.40.0; RRID: SCR_021322; ref. 31), and the data were visualized using deepTools (version 3.5.1; RRID: SCR_016366; ref. 29). Gene alignments were examined using Integrative Genomics Viewer (RRID: SCR_011793), and motif analysis was conducted using HOMER software. Visualizations were enhanced using custom R scripts and the Adobe Illustrator (RRID: SCR_010279).

Immunoblotting and IP analysis

Protein extracts were prepared using RIPA lysis buffer supplemented with a protease inhibitor cocktail (Roche) and quantified using the Pierce BCA Protein Assay (Thermo Fisher Scientific). The lysates, along with a prestained molecular weight marker (Thermo Fisher Scientific, cat. #26616), were resolved by SDS-PAGE and transferred to a nitrocellulose membrane for immunoblotting analysis. For IP, 5×10^6 cells were lysed in IP lysis buffer (Beyotime Biotechnology) containing a protease inhibitor cocktail and incubated on ice for 30 minutes. Anti-FLAG antibody (Sigma-Aldrich, cat. #F3165; RRID: AB_259529) was used for IP. Precleared lysates were incubated with 8 μg anti-FLAG antibody at 4°C for 4 hours, followed by overnight incubation with protein A/G Dynabeads (MedChemExpress, cat. #HY-K0202) at 4°C. After washing with IP buffer, the immunoprecipitates were boiled in SDS sample buffer and analyzed using immunoblotting. The NuRD Complex Antibody Sampler Kit (Cell Signaling Technology, cat. #8349T) was used for immunoblotting the NuRD complex components.

Animal experimentation

All mouse experiments were conducted at the Tsinghua University Animal Experiment Center in compliance with protocols approved by the Institutional Animal Care and Use Committee of Tsinghua University (protocol number: 19-PD-1).

Subcutaneous tumor model

The 4T1 cells (2×10^5) were injected subcutaneously into the flanks of mice. Female BALB/c mice (RRID: MGI:2683685), ages 8 to 12 weeks, were used for both the wild-type (WT) and CD8 depletion groups. For the CD8 depletion group, mice ($n = 6$) were administered 100 μg/mouse of CD8b mAb (Bio X Cell mAb, clone 53-5.8, cat. #BE0223) on day −1, day 0, and then every 4 days thereafter. Additionally, 8–18-week-old NOD/SCID gamma (NSG) mice (RRID: IMSR_JAX:005557) were included in the study. Tumor length and width were measured every 3 days once the tumors became palpable, and tumor volume was calculated using the formula: (length × width^2)/2. The experimental endpoint was reached when the tumor diameter reached 2.0 cm or when the mice died. Where feasible, investigators were blinded to sample allocations during tumor size measurements.

Lung metastasis model

The 4T1 cells (2×10^5) were injected intracardially into the tail veins of female BALB/c mice (RRID: MGI:2683685) of 8 to 12 weeks of age. Mice were divided into WT, NK cell–depleted, and CD8$^+$ T-cell–depleted groups. For CD8 depletion ($n = 6$), 100 μg/mouse of CD8b mAb (Bio X Cell mAb, clone 53-5.8, cat. #BE0223) was administered intraperitoneally on day −1, day 0, and every 3 days thereafter. For NK cell depletion ($n = 6$), 50 μL/mouse of the anti–ASGM-1 antibody (FUJIFILM Wako, cat. #014-09801; RRID: AB_3678835) was administered intraperitoneally on day −1 and day

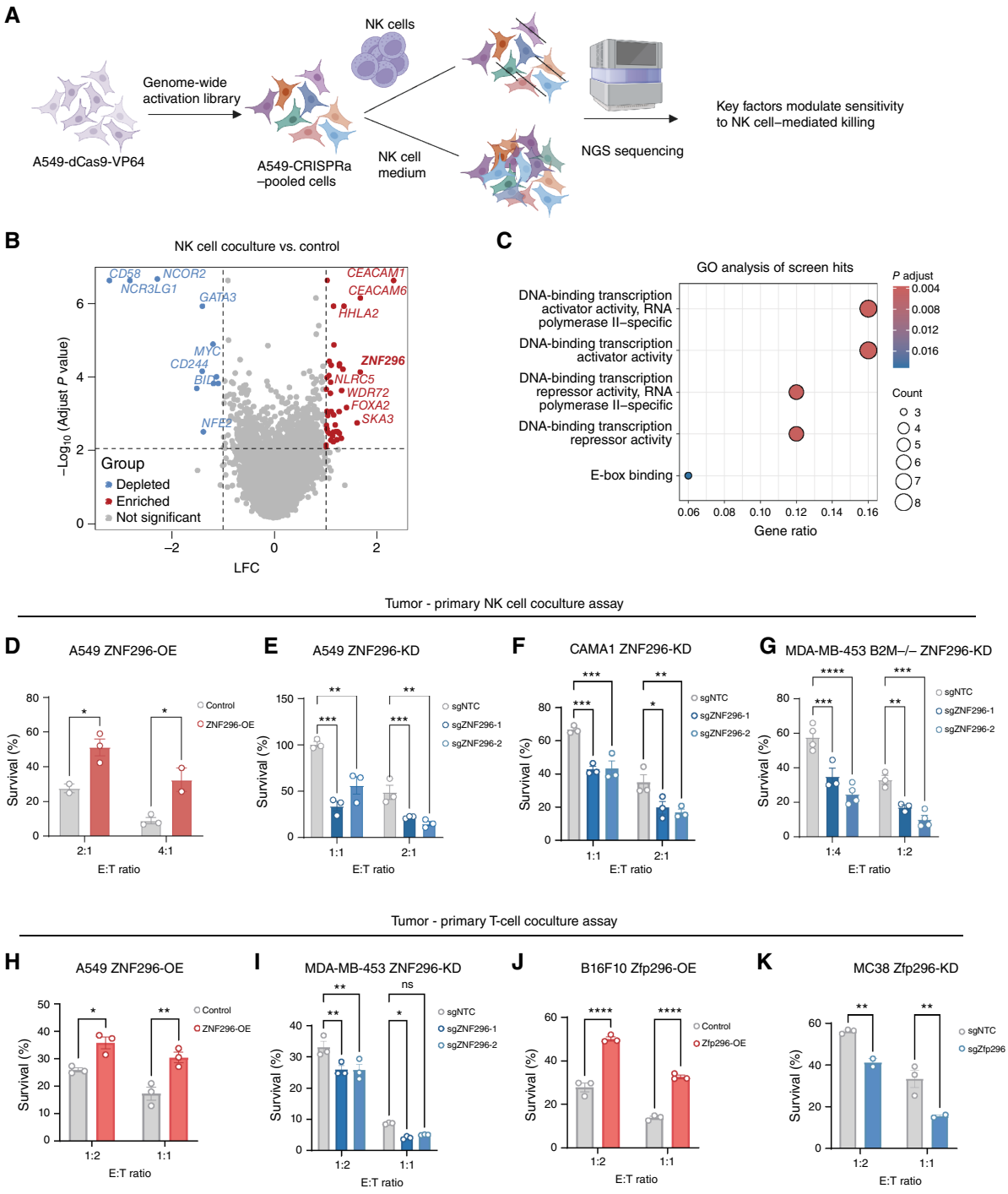

Figure 1.

Genome-wide CRISPRa screen identifies ZNF296 as a major TF suppressing antitumor immunity. **A,** Schematic presentation of the CRISPRa screen in A549 cells cocultured with NK-92MI. NGS, next-generation sequencing. **B,** Volcano plot showing genes with enriched and depleted sgRNAs in the NK-92MI coculture group compared with the control group without NK cells. **C,** GO analysis of top screening hits [−log (adjusted *P* value) > 2 and |LFC| > 1] that regulate sensitivity to NK cell–mediated killing. **D,** Control and ZNF296-OE A549 cells, driven by the PGK promoter, were cocultured with primary NK cells at E:T ratios of 2:1 and 4:1. **E** and **F,** Control (sgNTC) and ZNF296-KD (sgZNF296-1/-2) A549 cells (**E**) and CAMA1 cells (**F**) were cocultured with primary NK cells at E:T ratios of 1:1 and 2:1. **G,** Control and ZNF296-KD MDA-MB-453 B2M knockout cells (sgZNF296-1/-2) were cocultured with primary NK cells at E:T ratios of 1:4 and 1:2. **H** and **I,** Control and ZNF296-OE A549 cells (**H**) or control and ZNF296-KD MDA-MB-453 cells (**I**), ectopically expressing NY-ESO-1 and HLA-A*02, were cocultured with primary T cells engineered to express NY-ESO-1–specific TCRs at E:T ratios of 1:2 and 1:1. **J** and **K,** Control and Zfp296-OE (*Continued on the following page.*)

0, followed by 50 μL/mouse every 3 days. Additionally, 8–18-week-old NSG mice were included in the study. NSG mice were harvested on day 15, whereas NK cell–depleted, $CD8^+$ T-cell–depleted, and WT mice were harvested on day 18. Lungs containing tumor nodules were excised and fixed in modified Bouin's fixative solution. Hematoxylin and eosin staining was then conducted, and images were acquired using the Axio Scan.Z1 Zeiss fully automated digital slide scanner.

Analysis of tumor-infiltrating lymphocytes

Tumors were dissociated using the gentleMACS dissociator in a solution containing 1 mg/mL collagenase type IV (Sigma-Aldrich, C5138), 20 U/mL DNase type IV (Sigma-Aldrich, D5205), and 0.1 mg/mL hyaluronidase type V (Sigma-Aldrich, H6254) for 30 minutes at 37°C. The resulting cell suspension was passed through a 70-μm filter to obtain single cells, with a small fraction used for flow cytometry. Cells were first stained using the LIVE/DEAD Fixable Near-IR Dead Cell Stain Kit (Thermo Fisher Scientific, cat. #L34975) in PBS and subsequently blocked with anti–mouse CD16/32 (BioLegend, cat. #101320; RRID: AB_1574975) to prevent nonspecific binding to the IgG Fc receptor. For intracellular staining, cells were fixed and permeabilized using an Intracellular Fixation & Permeabilization Buffer Set (Thermo Fisher Scientific, cat. #88-8824-00). The following antibodies were used for tumor-infiltrating lymphocyte staining: anti–mouse CD45 (BioLegend, cat. #103108; RRID: AB_312973), anti–mouse CD3 (BioLegend, cat. #100204; RRID: AB_312661), anti–mouse CD8a (BioLegend, cat. #100708; RRID: AB_312747), anti–mouse CD4 (BioLegend, cat. #100559; RRID: AB_2562608), anti–mouse NKp46 (BioLegend, cat. #137608; RRID: AB_10612758), and anti–granzyme B (BioLegend, cat. #372214; RRID: AB_2728381). Data were collected using Beckman Coulter CytoFLEX S and analyzed using FlowJo software (RRID: SCR_008520).

Cell growth and viability

For cell growth and viability experiments *in vitro*, 2,000 cells were plated in 96-well plates, and live cells were quantified using CellTiter-Glo Luminescent Cell Viability Assay (Beyotime Biotechnology, cat. #C0065) according to the manufacturer's instructions. Luminescence was measured using a microplate reader to quantify metabolically active cells.

Statistical analysis

Statistical analyses were performed using GraphPad Prism 9 software (RRID: SCR_002798), and values were expressed as mean ± SEM of independent biological replicates. An unpaired Student *t* test and a one-way ANOVA or two-way ANOVA test were used as indicated (ns, not significant; *, $P < 0.05$; **, $P < 0.01$; ***, $P < 0.001$; ****, $P < 0.0001$). For power analysis, the group sizes for *in vivo* experiments were determined empirically based on prior experience with the corresponding tumor models. Similarly, *in vitro* group sizes were selected based on our prior knowledge of the variation in the experiments.

Results

Genome-wide CRISPR activation screen identifies ZNF296 as a key regulator of resistance to killing mediated by NK and cytotoxic T cells

To identify genes that modulate sensitivity to NK-mediated killing, we conducted a genome-wide CRISPR activation (CRISPRa) screen in the lung cancer cell line A549 cocultured with NK cells. In this screening, A549 cells were first engineered to express dCas9-VP64, followed by infection with a genome-wide sgRNA library to activate specific genes. The CRISPR-perturbed tumor cells were then cocultured with NK-92MI cells, a highly cytotoxic NK-like cell line (**Fig. 1A**; refs. 34, 35). Genes, the expression of which increased in sensitivity to NK cell–mediated killing, were identified by the depletion of corresponding sgRNAs. Notably, these genes included known NK cell–activating ligands such as *NCR3LG1* (encoding B7-H6) and *CD58*, as well as inhibitory ligands *CEACAM1* and *CEACAM6*, confirming screen validity (**Fig. 1B**), suggesting that our screen successfully recapitulated known regulators of sensitivity to NK cell–mediated killing.

Subsequently, GO analysis of the top screening hits revealed that many of these factors are involved in DNA binding and gene regulation (**Fig. 1C**), suggesting a pivotal role for transcriptional regulation in modulating NK cell–mediated killing. Among these TFs, ZNF296, a poorly characterized zinc-finger protein with DNA-binding activity, showed the most significant enrichment (**Fig. 1B**; Supplementary Fig. S1A), indicating its potential role in the regulation of NK cell–mediated killing.

To validate ZNF296 function, we first overexpressed it in A549 cells via CRISPRa using two sgRNAs. Coculture with NK-92MI cells confirmed that ZNF296 overexpression conferred resistance to NK-mediated killing (Supplementary Fig. S1B). Additionally, we ectopically expressed ZNF296 cDNA under the control of the PGK promoter in A549 cells and found that ZNF296 expression substantially conferred resistance to NK-mediated killing (Supplementary Fig. S1C–S1E). To further validate our findings, we cocultured cancer cells with primary NK cells isolated from healthy donors. We observed that ZNF296 overexpression conferred resistance to killing by primary NK cells (**Fig. 1D**).

Complementary to the gain-of-function approach, we investigated whether inhibiting ZNF296 could sensitize tumors to NK cell–mediated cytotoxicity. Consistently, the suppression of ZNF296 expression in A549 cells using the CRISPR interference approach significantly increased their sensitivity to NK cell–mediated killing (**Fig. 1E**; Supplementary Fig. S1F). We also examined this effect in two additional breast cancer cell lines, CAMA1 and MDA-MB-453, both of which exhibit high ZNF296 expression (Supplementary Fig. S1G). Similar to the results in A549 cells, ZNF296 KD in CAMA1 enhanced sensitivity to NK cell–mediated killing (**Fig. 1F**; Supplementary Fig. S1H). MDA-MB-453 cells were less sensitive to NK cell–mediated killing. To enhance their sensitivity, we first knocked out B2M to deplete the HLA molecules. In B2M knockout MDA-MB-453 cells, the suppression of ZNF296 resulted in increased sensitivity to NK cell–mediated killing (**Fig. 1G**; Supplementary Fig. S1I).

(*Continued*.) B16F10 cells (**J**) or control and Zfp296-KD MC38 cells (**K**) were pulsed with SIINFEKL peptide and cocultured with OT-I T cells at E:T ratios of 1:2 and 1:1. Data are represented as mean ± SEM across $n = 2$–4 replicates (**D–K**). ns, not significant; *, $P < 0.05$; **, $P < 0.01$; ***, $P < 0.001$; ****, $P < 0.0001$ by two-way ANOVA (**D–K**). Data are representative of two independent experiments (**D–K**). **A,** Created in BioRender. Pan, D. (2025) https://BioRender.com/evdr16g.

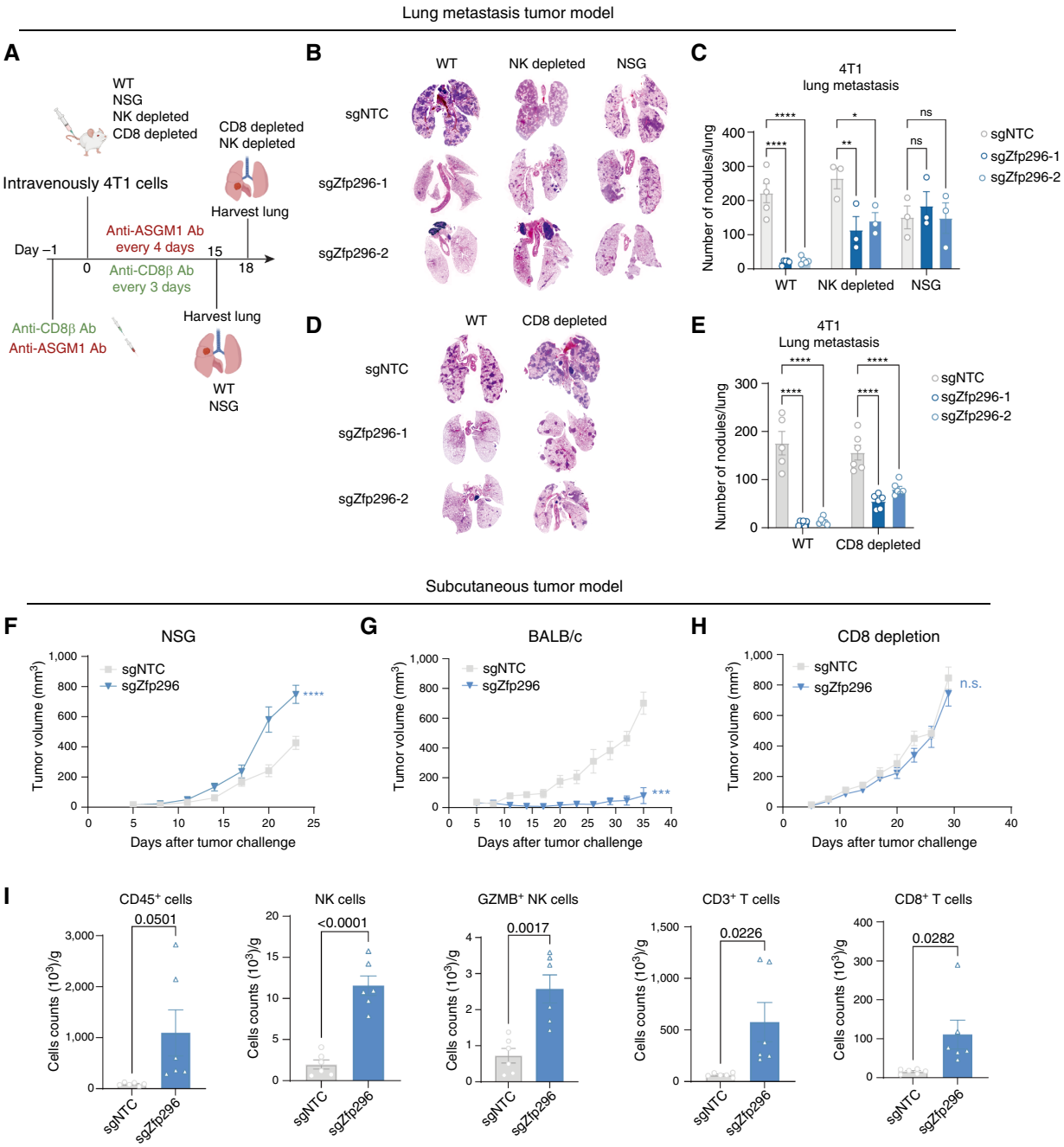

Figure 2.

Inhibition of Zfp296 suppresses tumor growth and enhances antitumor immune response. **A,** Schematic of the 4T1 lung metastasis tumor model. **B** and **C,** Representative hematoxylin and eosin staining (**B**) and quantification (**C**) of lung metastatic nodules from WT, NK cell–depleted, and NSG mice injected with control or Zfp296-KD 4T1 cells. **D** and **E,** Representative hematoxylin and eosin staining (**D**) and quantification (**E**) of lung metastatic nodules from WT and CD8 cell–depleted mice injected with control and Zfp296-KD 4T1 cells. **F–H,** Tumor growth curves of control and Zfp296-KD 4T1 cells in NSG mice (**F**), WT (**G**), and CD8 T–cell depleted (**H**) BALB/c mice. **I,** Quantification of immune cell infiltration in tumors from mice injected with control and Zfp296-KD 4T1 cells, analyzed using flow cytometry. The number of $CD45^+$ cells, NK cells ($CD3^-NKp46^+$), $GZMB^+$ NK cell, $CD3^+$ T cells, and $CD8^+$ T cells was determined per gram of tumor. Data are represented as mean ± SEM. NK cell–depleted and NSG mice ($n = 3$ replicates) and WT mice ($n = 5$ replicates; **C**); WT and $CD8^+$ T-cell–depleted mice ($n = 6$ replicates; **E**); across $n = 6$ replicates (**F–I**). ns, not significant; *, $P < 0.05$; **, $P < 0.01$; ****, $P < 0.0001$ by two-way ANOVA (**C** and **E–H**) and unpaired Student t test (**I**).

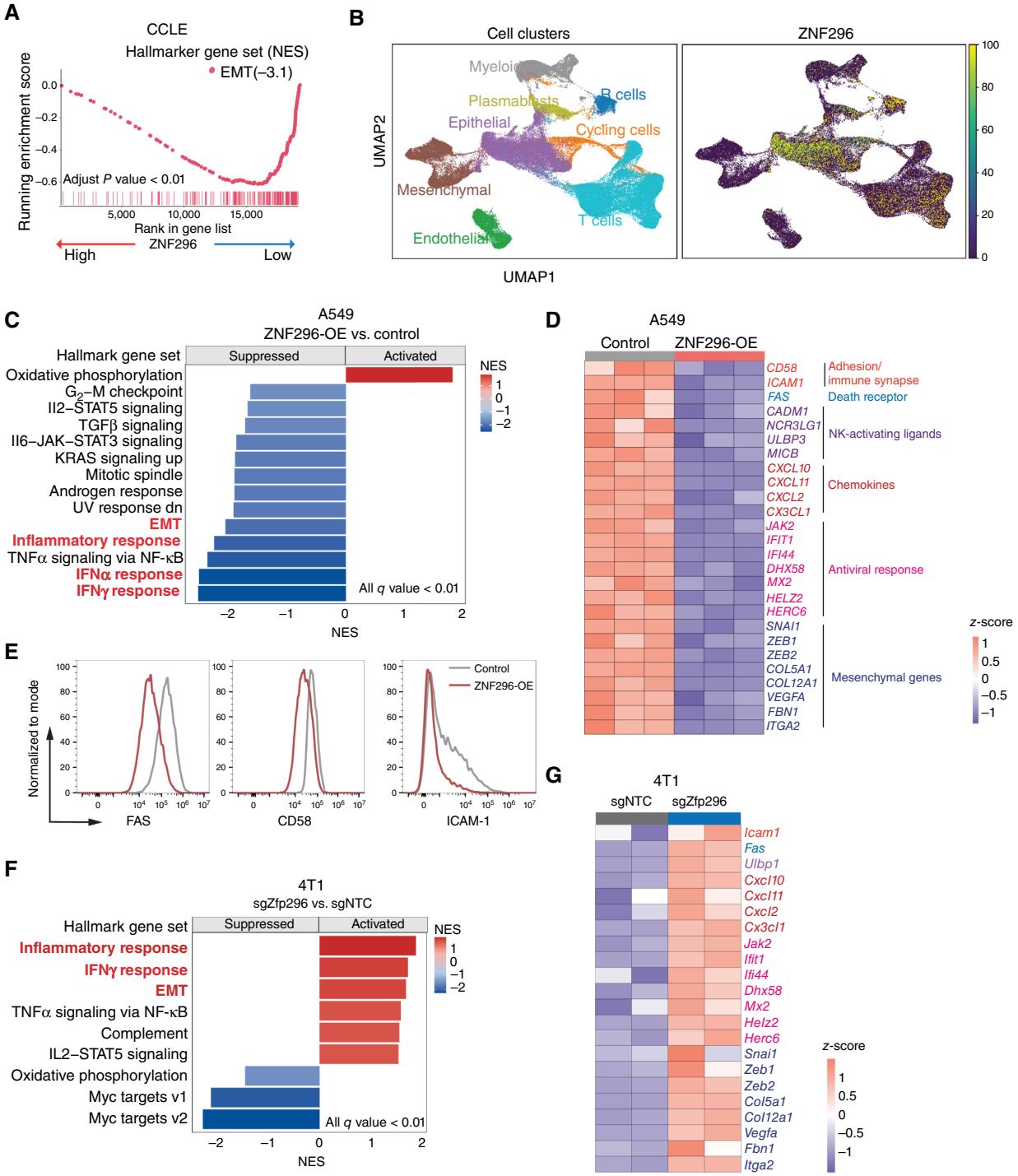

Figure 3.

ZNF296 is highly expressed in epithelial cells that suppress IFN response and EMT program. **A,** GSEA was performed using the Cancer Cell Line Encyclopedia (CCLE) dataset, ranking genes by their correlation with ZNF296 expression across 1,377 cell lines. High ZNF296 expression is negatively associated with hallmark gene set EMT [normalized enrichment scale (NES) = −3.1; $P < 0.01$]. **B,** Uniform Manifold Approximation and Projection (UMAP) plots from the dataset GSE176078 show cell-type clustering (left) and ZNF296 expression levels (right) across immune and tumor cell populations. **C,** GSEA of ZNF296-OE A549 cells identified significantly altered hallmark gene sets ($P < 0.01$), color-coded by normalized enrichment scale. **D,** Heatmap showing differentially expressed genes following ZNF296 overexpression, which is relevant to IFN response, inflammatory response, and EMT program genes. **E,** Flow cytometry of ZNF296-OE and control A549 cells showing the expression of NK ligands FAS, CD58, and ICAM-1. **F,** GSEA of Zfp296-KD 4T1 cells identified significantly enriched hallmark gene sets ($P < 0.01$), color-coded by normalized enrichment scale. **G,** Heatmap showing differentially expressed genes following Zfp296 KD, which is relevant to IFN response, inflammatory response, and EMT program genes.

Building on these findings, we next sought to determine whether ZNF296 modulates sensitivity to T-cell–mediated killing, given that T cells are key effectors of antitumor immunity. Consistent with the results from NK cell cocultures, ZNF296-OE A549 cells exhibited an increase in resistance to T-cell–mediated killing, whereas ZNF296 KD in MDA-MB-453 cells modestly increased the sensitivity to T-cell–induced killing (**Fig. 1H** and **I**). To further validate these findings in a murine system, we employed the OVA/OT-1 antigen-specific model using the mouse tumor cell lines B16F10 and MC38. Overexpression of Zfp296 in B16F10 cells conferred increased resistance to OT-1 T-cell–mediated killing (**Fig. 1J**; Supplementary Fig. S1J). Conversely, Zfp296 KD in MC38 sensitized the tumor cells to OT-1 T-cell cytotoxicity (**Fig. 1K**; Supplementary Fig. S1K). These findings establish that ZNF296 is a key TF that confers resistance to both NK and T-cell–mediated cytotoxicity in multiple cell models.

Inhibition of Zfp296 enhances NK and T-cell–mediated antitumor immunity *in vivo*

Next, we evaluated the immunomodulatory role of ZNF296 in mouse tumor models. To this end, we knocked down *Zfp296* (the murine homolog of ZNF296) in 4T1 cells, a breast cancer cell line known to have high endogenous Zfp296 expression. We first performed a coculture assay consisting Zfp296 KD 4T1 cells and

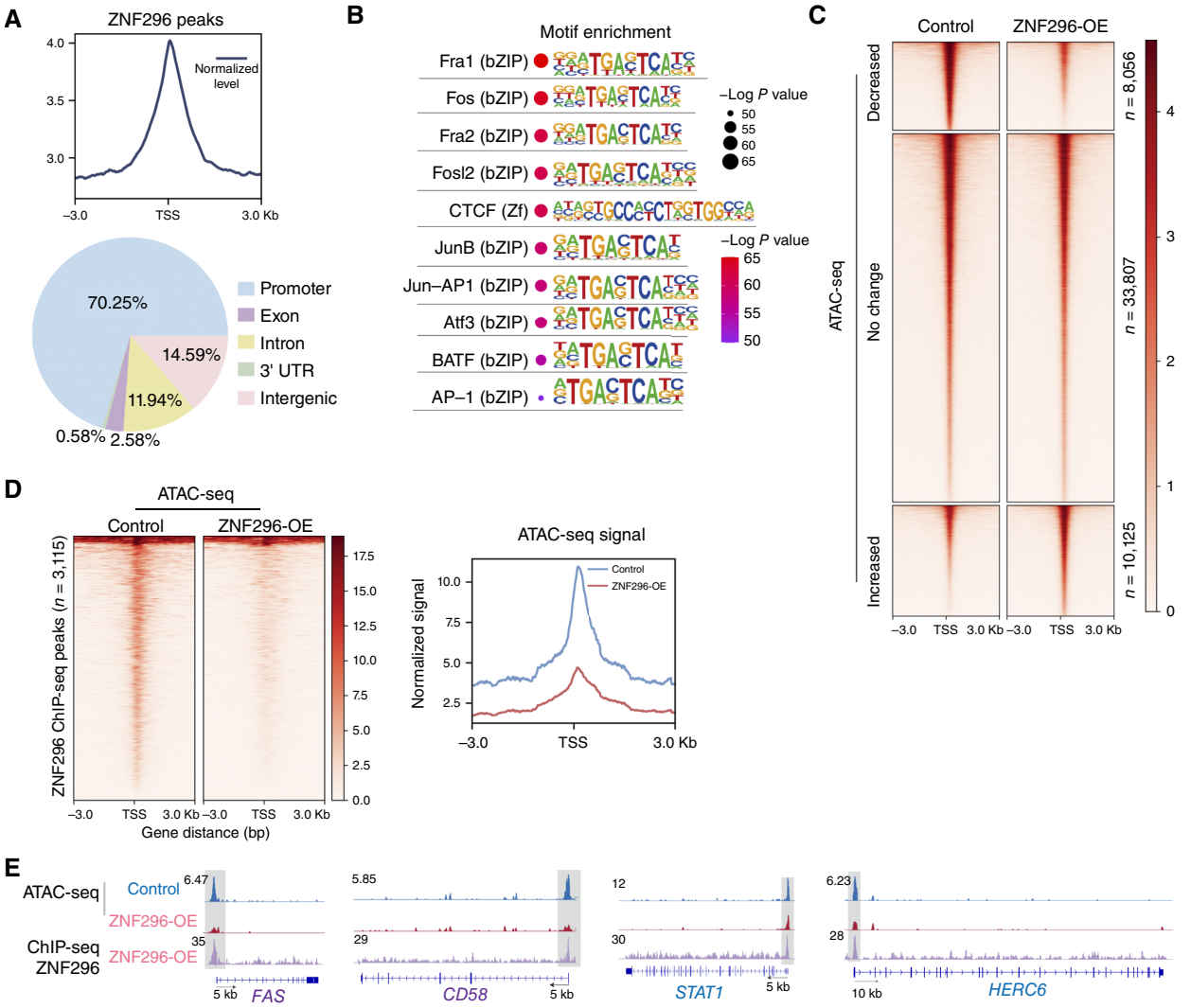

Figure 4.

ZNF296 directly binds to the promoters of target genes and mediates the suppression of chromatin accessibility. **A,** Top, plot showing the distribution of ZNF296-Flag ChIP-seq peaks relative to known transcription start site (TSS). Bottom, pie plot showing the genomic distribution of ZNF296-Flag ChIP-seq peaks in A549 cells. UTR, untranslated region. **B,** Top 10 enriched motifs identified from ZNF296-Flag ChIP-seq peaks, analyzed, and *P* values calculated using HOMER software. **C,** Heatmap displaying the density of ATAC-seq reads comparing ZNF296-OE A549 cells with control cells. **D,** Left, heatmap plots displaying ATAC-seq read distribution at ZNF296-Flag binding regions (±3 kb from transcription start site) in control and ZNF296-OE A549 samples. Right, line plots showing the normalized ATAC-seq signals of transcription start site regions of the ZNF296-binding sites. **E,** Genome browser tracks displaying ZNF296 ChIP-seq in ZNF296-OE and ATAC-seq data in both ZNF296-OE and control A549 cells at the genomic loci of several genes: *FAS*, *CD58*, *STAT1*, and *HERC6*. Tracks for ATAC-seq were generated from merged replicates ($n = 3$ per group) and normalized using counts per million.

murine NK cells. We showed that the KD of Zfp296 similarly enhanced NK cell–mediated killing, consistent with observations using human cell lines (Supplementary Fig. S2A and S2B). We then performed an experimental lung metastasis assay by intravenously injecting either control or Zfp296 KD 4T1 cells, with or without NK depletion (**Fig. 2A**; Supplementary Fig. S2C). This model was

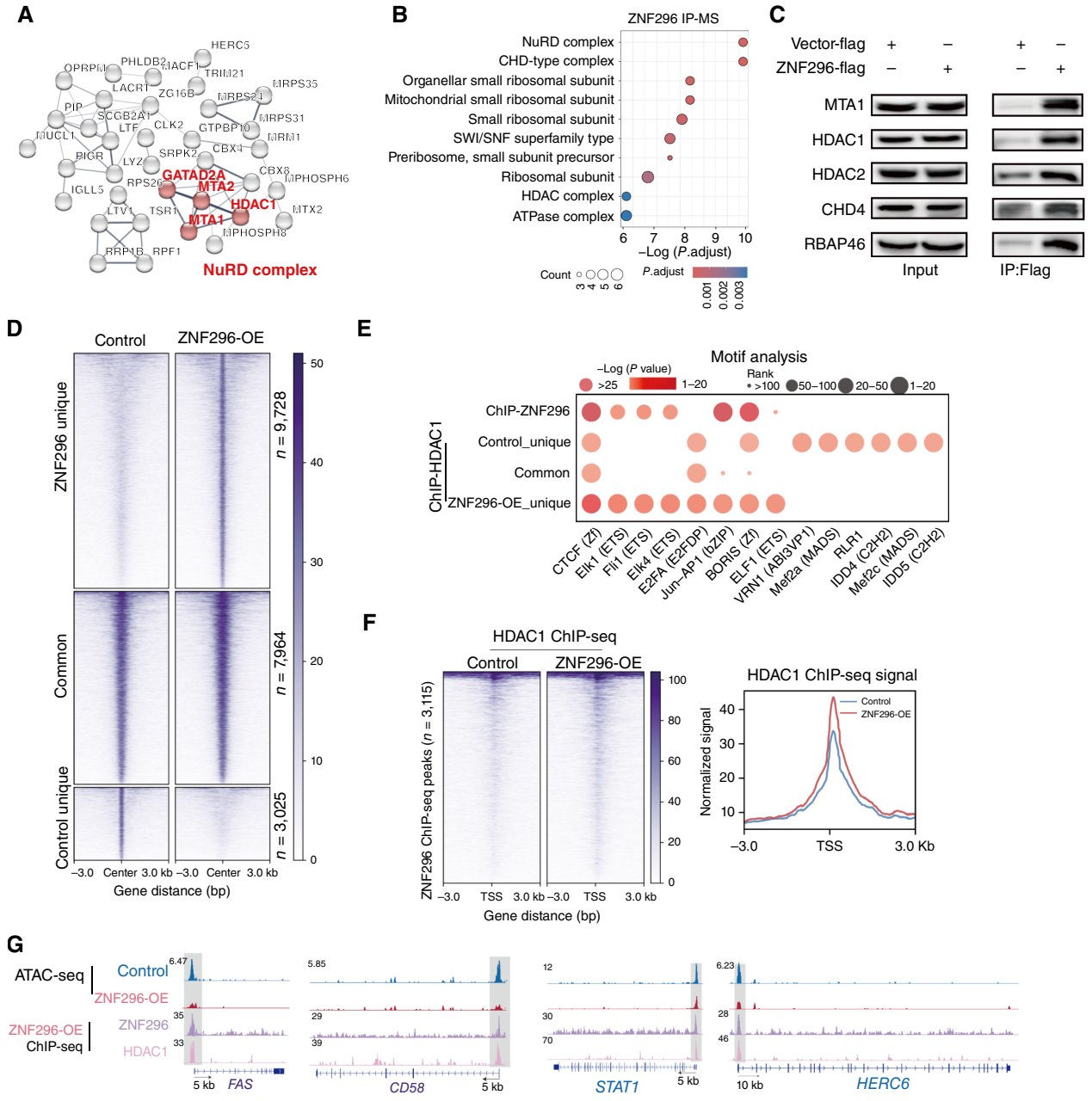

Figure 5.

ZNF296 recruits the NuRD complex to suppress target gene expression and drive resistance to NK cell–mediated killing. **A** and **B,** STRING network (**A**) and GO analysis (**B**) of ZNF296-interacting proteins identified through mass spectrometry (MS). **C,** Coimmunoprecipitation of ZNF296 using an anti-FLAG antibody in ZNF296-flag–expressed A549 cells, followed by Western blot detection of NuRD complex components. **D,** Heatmaps displaying the density of HDAC1 ChIP-seq reads at ZNF296-OE–unique, control-unique, and common HDAC1-binding peaks in control and ZNF296-OE A549 cells. **E,** Enriched motifs identified in regions of HDAC1 binding that are unique to the ZNF296-OE sample (ZNF296-OE–unique), unique to the control sample (control-unique), and shared between both samples (common), as shown in **D**. **F,** Left, heatmap showing the HDAC1 ChIP-seq signal at ZNF296 ChIP-seq peaks (n = 3,115) in ZNF296-OE and control A549 cells, centered on ±3 kb from transcription start site. Right, line plot showing the normalized HDAC1 ChIP-seq signal in ZNF296-OE (red) and control (blue) A549 cells. **G,** Genome browser tracks displaying HDAC1 ChIP-seq, ZNF296 ChIP-seq in ZNF296-OE, and ATAC-seq signals in both ZNF296-OE and control A549 cells. Shown are the loci of NK/T ligands: *FAS*, *CD58*, *STAT1*, and *HERC6*. Tracks for ATAC-seq were generated from merged replicates (n = 3 per group) and normalized using counts per million. TSS, transcription start site.

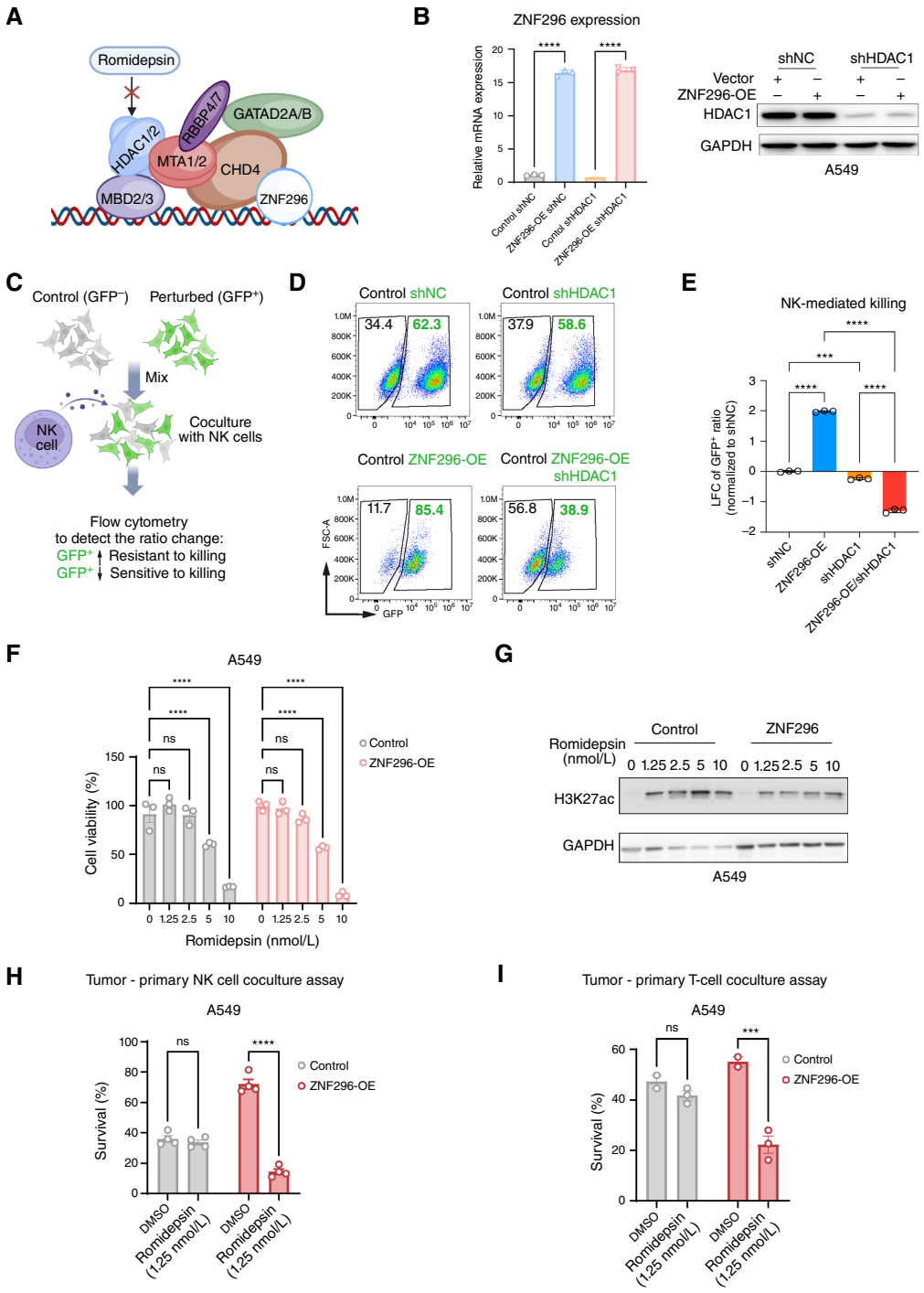

Figure 6.

Inhibition of NuRD complex activity sensitizes ZNF296 high expression tumor cell to NK cell–mediated killing. **A,** Schematic of the NuRD complex. **B,** Left, qPCR analysis of ZNF296 levels in control and ZNF296-OE A549 cells with either nontargeting shRNA (shNC) or HDAC1-targeting shRNA (shHDAC1). Right, Western blot analysis of HDAC1 protein levels in the same groups. **C,** Schematic of the coculture experiment to assess the role of HDAC1 in ZNF296-mediated resistance to NK-cell killing. GFP$^+$ A549 cells (control or ZNF296-OE, with shNC or shHDAC1) were mixed at 1:1 with GFP$^-$ WT A549 cells and cocultured with NK-92MI cells. GFP$^+$/GFP$^-$ ratio was analyzed using flow cytometry to determine the relative sensitivity to NK cell–mediated killing. **D,** Representative flow cytometry plots showing the GFP$^+$ cell proportions in the indicated groups after coculture with NK-92MI cells, as described in **C**. **E,** Bar graph showing the LFC of GFP$^+$ cell ratio (normalized to shNC) in shNC, ZNF296-OE, shHDAC1, and ZNF296 OE/shHDAC1 cells after NK cell coculture. **F,** Cell viability of A549 control and ZNF296-OE cells treated with romidepsin (1.25–10 nmol/L, 48 hours) measured using the CellTiter-Glo assay. **G,** Western blot analysis of H3K27ac and GAPDH after romidepsin treatment. **H,** Flow cytometry analysis of cell survival after NK coculture (E:T = 1:1) with or without (*Continued on the following page.*)

chosen because NK cells are key mediators controlling lung metastasis (2, 36, 37). Strikingly, Zfp296 KD significantly reduced the number of metastatic colonies. In contrast, NK-cell depletion partially restored the number of metastatic colonies, whereas the phenotype was fully rescued when tumor cells were injected into NSG mice, which lacked both NK and T cells (**Fig. 2B** and **C**). These findings indicate that Zfp296 KD cells are sensitive to NK cell–mediated immune surveillance and may also be susceptible to adaptive antitumor responses, such as T-cell–mediated immunity. To further confirm the potential involvement of T-cell–mediated immunity to Zfp296 KD tumors, we performed lung metastasis experiments in the presence or absence of $CD8^+$ T cells (Supplementary Fig. S2D). As expected, depletion of $CD8^+$ T cells also partially rescued the number of lung metastatic colonies, indicating that Zfp296 KD tumors are more susceptible to both NK and T-cell–mediated immunity in the 4T1 mouse model (**Fig. 2D** and **E**).

We next evaluated the effect of Zfp296 inactivation in a subcutaneous 4T1 tumor model, in which $CD8^+$ T cells play a relatively more important role in tumor control than in the lung metastasis model. Interestingly, although Zfp296 KD tumors grew at a similar rate as control tumors *in vitro* (Supplementary Fig. S2E), they exhibited accelerated growth in NSG mice, which may be attributed to enhanced EMT and NF-κB signaling. In contrast, Zfp296 KD markedly suppressed tumor growth in immunocompetent BALB/c mice, suggesting that Zfp296 inactivation elicited a robust antitumor immune response (**Fig. 2F** and **G**). We also observed suppression of tumor growth by Zfp296 KD in the MC38 subcutaneous model (Supplementary Fig. S2F). This antitumor response was largely dependent on $CD8^+$ T cells in the subcutaneous model, as administration of CD8 depletion antibodies resulted in similar tumor growth between Zfp296 KD and control cells in the 4T1 model (**Fig. 2H**). We then analyzed tumor-infiltrating immune cells in Zfp296 KD models. Strikingly, we observed a substantial increase in the levels of total infiltrated $CD45^+$ immune cells, including $CD8^+$ T cells and NK cells, within Zfp296 KD tumors, suggesting that Zfp296 KD induces an inflamed tumor microenvironment (TME; **Fig. 2I**; Supplementary Fig. S2G). Although the overall number of $CD8^+$ T cells increased significantly, the proportions of effector (GZMB+), progenitor (Ly108+ PD-1+), and terminally exhausted (Tim3+ PD-1+) $CD8^+$ T-cell subsets remained unchanged (Supplementary Fig. S2H and S2I). In addition, we examined the proportions of immunosuppressive myeloid subsets in the TME, including tumor-associated neutrophils ($CD11b^+$ $Ly6G^+$), immunomodulatory tumor-associated macrophages ($MHC\text{-}II^+$ $CX3CR1^+$), and proangiogenic tumor-associated macrophages ($MHC\text{-}II^-$ $CX3CR1^-$; ref. 38). No significant differences were observed in the frequencies of these myeloid populations between control and Zfp296 KD tumors (Supplementary Fig. S2J and S2K). Together, these results suggest that although Zfp296 inhibition enhances overall immune infiltration in tumors, it does not significantly affect the myeloid compartment.

ZNF296 is highly expressed in epithelial cells that suppress both mesenchymal program and IFN response gene expression

To better characterize ZNF296, we first examined its expression pattern in human cancers. Analysis of The Cancer Genome Atlas dataset showed that ZNF296 is broadly upregulated across various cancer types compared with normal tissues, suggesting a potential role in tumor progression (Supplementary Fig. S3A). Further analysis of the Cancer Cell Line Encyclopedia revealed a strong inverse correlation between ZNF296 expression and EMT program (**Fig. 3A**). Consistently, scRNA-seq data from a breast cancer cohort revealed higher ZNF296 expression in epithelial cells compared with mesenchymal cells (**Fig. 3B**). Together, these findings indicate that ZNF296 is highly expressed in epithelial cancer.

To identify the genes regulated by ZNF296, we performed RNA-seq analysis on ZNF296-OE A549 cells. Strikingly, ZNF296 overexpression suppressed several key pathways associated with antitumor immunity, including the IFN response and inflammatory response pathways (**Fig. 3C**; Supplementary Fig. S3B). Specifically, it downregulated genes involved in immune synapse formation and adhesion between the tumor and NK/T cells (e.g., CD58 and ICAM-1), chemokines that attract T cells and NK cells (e.g., CXCL10), and many genes involved in antiviral responses—a "viral mimicry" state previously linked to enhanced antitumor immunity (**Fig. 3D**; Supplementary Fig. S3C; ref. 39). Flow cytometry analysis revealed that FAS levels were substantially reduced upon ZNF296 overexpression, with modest reductions in CD58 and ICAM-1 (**Fig. 3E**; Supplementary Fig. S3D). Similarly, FAS, CD58, and ICAM-1 levels were elevated, albeit modestly for CD58 and ICAM-1, upon ZNF296 KD in MDA-MB-453 cells (Supplementary Fig. S3E). Furthermore, qPCR analysis showed that ZNF296 KD in CAMA1 cells enhanced the expression of IFN response genes, whereas Zfp296 overexpression in murine tumor cells suppressed these genes (Supplementary Fig. S3F and S3G). In addition to the IFN response, ZNF296 overexpression strongly suppressed the mesenchymal gene expression program, with EMT emerging as one of the top downregulated pathways (**Fig. 3C** and **D**; Supplementary Fig. S3B and S3C), consistent with its high expression in epithelial cells. To further validate these changes in the transcriptome, we performed RNA-seq on Zfp296 KD 4T1 tumor cells. Consistent with the data from A549 cells, GSEA revealed robust activation of the IFN and inflammatory response pathways, as well as the mesenchymal gene expression program, upon Zfp296 KD (**Fig. 3F** and **G**; Supplementary Fig. S3H and S3I). Interestingly, Zfp296 KD slightly upregulated MHC-I expression (Supplementary Fig. S3J), in contrast to the downregulation typically associated with EMT (40, 41). These data suggest that ZNF296 plays a conserved role in suppressing the IFN response and mesenchymal programs.

ZNF296 directly binds to the promoters of target genes and mediates suppression of chromatin accessibility

To identify the direct target of ZNF296, we conducted ChIP-seq using anti-Flag antibodies in A549 cells expressing ZNF296-Flag. The ChIP-seq results revealed that ZNF296 predominantly binds to promoter regions, consistent with its expected role as a TF (**Fig. 4A**). Motif analysis showed that DNA motifs related to the AP-1 transcription family (e.g., Fos, Fra1, and Junb) were highly enriched at ZNF296-binding sites (**Fig. 4B**). To determine whether ZNF296 enhances or suppresses gene transcription, we performed ATAC-seq on ZNF296-OE and control cells,

(*Continued*.) romidepsin pretreatment (1.25 nmol/L). **I,** Flow cytometry analysis of survival of ZNF296-OE and control cells cocultured with TCR T cells (E:T = 1:2), with or without romidepsin pretreatment (1.25 nmol/L). Data are represented as mean ± SEM across $n = 3$ replicates (**B**, **E**, and **F**), $n = 4$ replicates (**H**), and $n = 2$–3 replicates (**I**). ns, not significant; ***, $P < 0.001$; ****, $P < 0.0001$ by one-way ANOVA (**B** and **E**) and two-way ANOVA (**F**, **H**, and **I**). **A,** Created in BioRender. Pan, D. (2025) https://BioRender.com/1nyeock.

identifying differentially accessible peaks (Supplementary Fig. S4A and S4B). ATAC-seq identified 8,056 chromatin sites with decreased accessibility and 10,125 regions with increased accessibility upon ZNF296 overexpression (**Fig. 4C**). Strikingly, we observed a substantial reduction in chromatin accessibility at these ZNF296-binding sites, indicating that ZNF296 functions as a transcriptional suppressor by directly repressing target gene expression (e.g., *FAS*, *CD58*, *STAT1*, and *HERC6*; **Fig. 4D** and **E**). These findings indicate that ZNF296 acts as a transcriptional suppressor by binding to the promoter regions of specific target genes, reducing their chromatin accessibility, and consequently downregulating their expression.

ZNF296 interacts with the NuRD complex and HDAC1 to regulate target gene expression

Given that ZNF296 contains a C2H2 zinc-finger domain typical of DNA-binding proteins, we hypothesized that it might function in concert with other chromatin-modifying proteins to regulate gene expression. To identify potential interacting partners, we performed IP of ZNF296 followed by mass spectrometry. Network and GO analyses of ZNF296-interacting proteins identified key components of nucleosome remodeling and the HDAC (NuRD) complex, including GATAD2A, MTA1/2, and HDAC1, as significant interactors (**Fig. 5A** and **B**). These interactions were further validated by immunoblotting ZNF296 immunoprecipitates, confirming the presence of MTA1, HDAC1/2, CHD4, and RBAP46 (RBBP7) as NuRD components (**Fig. 5C**).

We hypothesized that ZNF296 suppresses target gene expression by recruiting the NuRD complex, which exerts HDAC activity through HDACs. To test this hypothesis, we conducted ChIP-seq analysis using antibodies against HDAC1, a key HDAC in the NuRD complex, in ZNF296-OE and control A549 cells. We identified 11,719 and 17,978 HDAC1 peaks in control and ZNF296-OE cells, respectively (Supplementary Fig. S5A). We then intersected these HDAC1 peaks and categorized them into three clusters: ZNF296-OE cell–unique HDAC1 sites (n = 9,728), control cell–unique HDAC1 sites (n = 3,025), and common HDAC1-binding sites (n = 7,964; **Fig. 5D**). Motif analysis of HDAC1-binding sites revealed that the unique HDAC1 sites in ZNF296-OE cells were closely aligned with the ZNF296-binding motif. In contrast, the unique HDAC1 sites in the control cells were enriched with a distinct set of motifs not bound by ZNF296 (**Fig. 5E**). These findings suggest that HDAC1 interacts with specific ZNF296-binding sites. Indeed, we observed increased HDAC1 signal at ZNF296-binding regions in ZNF296-OE cells compared with controls, with ZNF296 and HDAC1 colocalizing at key loci such as *FAS*, *CD58*, *STAT1*, and *HERC6* (**Fig. 5F** and **G**). Additionally, a substantial proportion of ZNF296-binding peaks overlapped with those of HDAC1, highlighting their co-occupancy at the genomic loci (Supplementary Fig. S5B). These findings suggested that ZNF296 interacts with the NuRD complex and exerts a suppressive effect on gene expression.

ZNF296 expression levels determine the sensitivity to HDAC1-mediated sensitization of NK and T-cell–mediated killing

We next sought to determine whether targeting the NuRD complex could reverse the immune suppression phenotype mediated by ZNF296 overexpression. HDAC1 is a key druggable component that mediates gene suppression in the NuRD complex (**Fig. 6A**). To this end, we generated A549 cells overexpressing ZNF296 (ZNF296-OE), HDAC1 KD cells via shRNA (HDAC1-KD), and a combination of ZNF296-OE/HDAC1-KD (**Fig. 6B**). After confirming a high efficiency of HDAC1 KD and ZNF296 overexpression, we prepared a mixture of WT control cells (GFP^-) and the aforementioned perturbed (GFP^+) A549 cells. These cells were then cocultured with NK cells for tumor killing, and their sensitivity to NK-mediated killing was assessed by measuring the ratio of GFP^+ to GFP^- cells (**Fig. 6C**). We found that ZNF296 overexpression conferred significant resistance to NK cell–mediated killing, consistent with our earlier findings (**Fig. 6D** and **E**). Although HDAC1-KD slightly increased the sensitivity to NK cell–mediated killing in control A549 cells, it substantially reversed the resistance phenotype induced by ZNF296-OE (**Fig. 6D** and **E**). Importantly, HDAC1 KD did not affect the proliferation of ZNF296-OE cells over the 24-hour period used for the NK coculture experiment, indicating that the observed effects were not due to changes in cell growth (Supplementary Fig. S5C). These results indicate that targeting HDAC1 can effectively resensitize ZNF296-OE cells to NK cell–mediated killing.

We further investigated whether pharmacologically targeting HDAC1 with romidepsin, an FDA-approved HDAC inhibitor, could sensitize ZNF296-OE tumor cells to NK and T-cell–mediated killing. As high doses of romidepsin can inhibit cell proliferation, we titrated the treatment in A549 cells and identified a low dose (1.25 nmol/L) of romidepsin that increased H3K27 acetylation levels without affecting cell proliferation (**Fig. 6F** and **G**). We then treated ZNF296-OE and control cells with 1.25 nmol/L romidepsin, followed by coculture with NK or T cells for specific killing assays. Strikingly, we found that although 1.25 nmol/L romidepsin treatment did not significantly affect NK or T-cell–mediated killing in control A549 cells, it substantially enhanced the sensitivity of ZNF296-OE cells to both NK and T-cell–mediated killing, consistent with our genetic data (**Fig. 6H** and **I**). These findings suggest that high ZNF296 expression renders tumor cells more responsive to NK and T-cell–mediated killing following even low-dose treatment with an HDAC inhibitor.

Discussion

In this study, we performed a genome-wide CRISPRa screen in A549 cells cocultured with NK cells and identified ZNF296 as a key TF, the overexpression of which drives resistance to NK cell–mediated killing. The role of ZNF296 in conferring resistance was further validated using both gain-of-function (overexpression) and loss-of-function (KD) approaches, supporting the robustness of our CRISPRa screen. Several prior studies have conducted large-scale loss-of-function screens in tumor cells cocultured with NK cells and identified important regulators of NK cell–mediated cytotoxicity (5, 6, 10, 14). However, ZNF296 did not emerge as a major hit in these NK cell–based screens or in other *in vivo* screens that primarily assess T-cell–mediated immunity. We reason that this difference is largely attributable to our use of a gain-of-function CRISPRa screen, which is particularly effective in detecting genes with low basal expression. Indeed, ZNF296 is expressed at low levels in many solid tumors but is highly expressed in certain epithelial cancer cells, such as the breast cancer models used for validation in this study. Consequently, loss-of-function screens may have limited sensitivity in detecting lowly expressed genes such as *ZNF296*. Notably, one prior study (13) employed a CRISPRa screen in lymphoma cell models, yet ZNF296 did not emerge as a top hit. This observation suggests that gene expression levels and genetic or epigenetic context are critical factors shaping NK-cell immune evasion

mechanisms. This may be especially relevant for ZNF296, the function of which seems to involve transcriptional repression through the NuRD complex.

ZNF296 modulates multiple gene expression programs in cancer cells. A major program upregulated upon ZNF296 KD is the IFN-stimulated gene (ISG) program, which is often associated with enhanced antitumor immune responses. Indeed, we showed that overexpression of ZNF296 consistently repressed ISG expression, whereas ZNF296 KD markedly increased ISGs, including key T-cell chemoattractants such as CXCL10. Correspondingly, ZNF296 KD led to a significant increase in immune cell infiltration, particularly $CD8^+$ T cells. These results indicate that the ZNF296–ISG axis may contribute to reshaping the TME. Second, ZNF296 also suppresses the EMT gene expression program. Previous studies have shown that the epithelial cell state is linked to resistance to NK cell–mediated killing (5, 16). Thus, ZNF296 could serve as a mechanistic link between EMT regulation and resistance to NK-mediated killing. Third, inactivation of ZNF296 seems to suppress Myc gene expression signatures and oxidative phosphorylation based on our RNA-seq analysis and GSEA. This suggests that ZNF296 may also regulate metabolism and Myc-mediated gene expression programs, although no apparent differences in cell proliferation were observed *in vitro* and even elevated tumor burden was noted in NSG mice (as discussed later). The detailed molecular mechanisms by which ZNF296 modulates these diverse gene expression programs and its complex effects on cancer cell malignancy remain to be experimentally elucidated in future studies.

We identified the NuRD complex as a key mediator of ZNF296-driven transcriptional repression, consistent with previous reports showing that ZNF296 specifically interacts with NuRD in embryonic stem cells (42). NuRD is a well-established epigenetic regulatory complex with essential roles in various biological processes, including embryonic development, stem cell maintenance, and tumor progression (43, 44). However, whether and how NuRD contributes to immune evasion remain less well understood. One study demonstrated that ZNF652 recruits the NuRD complex to repress PD-L1 in triple-negative breast cancer (45). Another study showed that RAD21 interacts with YAP/TEAD4 to recruit NuRD and suppress IFN signaling (46). These findings suggest that NuRD can facilitate immune evasion through its interaction with specific TFs depending on the context. Here, we demonstrated that ZNF296 physically interacts with the NuRD complex, a mechanism that is critical for enabling escape from T- and NK cell–mediated attacks and facilitating immune evasion in epithelial cancer cells.

Finally, we explored the therapeutic implications of ZNF296 in cancer treatment. Targeting ZNF296 seemed to potentiate antitumor immune responses based on our *in vivo* findings. However, in the 4T1 model, ZNF296 KD unexpectedly accelerated tumor growth in NSG mice (**Fig. 2**F), highlighting the complex role of ZNF296 in regulating tumor growth within the tumor immune microenvironment and suggesting that targeting ZNF296 may yield different outcomes depending on the host immune system. Indeed, as ZNF296 inactivation also upregulated the gene expression signature of EMT, a process often associated with metastasis, caution is warranted when considering direct ZNF296 inhibition. To address this, we investigated targeting HDAC, a core component of the NuRD complex, in the context of ZNF296 expression. We found that ZNF296 overexpression determined the therapeutic response to romidepsin, an HDAC1/2 inhibitor, particularly in enhancing NK-mediated killing. Notably, a low dose of romidepsin (1.25 nmol/L), which did not affect tumor cell viability or proliferation, was sufficient to substantially enhance T- and NK cell–mediated cytotoxicity in ZNF296-OE cells compared with controls. These findings provide a rationale for using low-dose HDAC inhibitors as a strategy to potentiate antitumor immunity while minimizing toxicity.

Data Availability

The scRNA-seq data analyzed in this study were obtained from GEO (GSE176078). Data supporting the conclusions of this study are available at GEO under the following accession numbers: RNA-seq data for ZNF296 overexpression in A549 and KD in 4T1 (GSE283056), ATAC-seq data for ZNF296 overexpression in A549 (GSE283057), and ChIP-seq data for ZNF296 and HDAC1 (GSE283059). ZNF296 expression data across various tumor types were obtained from TIMER2.0 at http://timer.cistrome.org/. ZNF296 expression data across various cell lines were obtained from DepMap at https://depmap.org/portal/. All other raw data are available upon request to the corresponding author.

Authors' Disclosures

D. Pan reports grants from Boehringer Ingelheim Pharmaceuticals, Bayer AG, and Sinopharm outside the submitted work. No disclosures were reported by the other authors.

Authors' Contributions

H. Wang: Conceptualization, data curation, software, formal analysis, validation, investigation, methodology, writing–original draft, writing–review and editing. **F. Zhao:** Conceptualization, formal analysis, validation, investigation, methodology, writing–original draft, writing–review and editing. **Y. Li:** Formal analysis, validation, investigation. **P. Wang:** Software, formal analysis, investigation, writing–review and editing. **Y. Wang:** Validation, investigation. **P. Ren:** Software, formal analysis. **C. Li:** Formal analysis. **H. Zheng:** Resources. **Z. Zeng:** Conceptualization, data curation, software, supervision, funding acquisition. **D. Pan:** Conceptualization, formal analysis, supervision, funding acquisition, project administration, writing–review and editing.

Acknowledgments

We thank Dr. Mo Chen (Tsinghua University) for sharing the pCRISPRi-v2 plasmid. We thank all members of the Pan and Zeng laboratories for their comments and suggestions. This work was supported by the National Natural Science Foundation of China grants (82341026 and 82073163; D. Pan), the National Key Research and Development Program of China (number 2022YFC2505400; D. Pan), the Tsinghua University Initiative Scientific Research Program (D. Pan), and the Tsinghua-Peking Joint Centre for Life Sciences (D. Pan and Z. Zeng). We would like to acknowledge the use of AI tools, specifically ChatGPT by OpenAI, for its assistance in language refinement and enhancing the clarity of the manuscript.

Note

Supplementary data for this article are available at Cancer Research Online (http://cancerres.aacrjournals.org/).

Received January 13, 2025; revised June 8, 2025; accepted September 18, 2025; posted first September 24, 2025.

References

1. Arner EN, Rathmell JC. Metabolic programming and immune suppression in the tumor microenvironment. Cancer Cell 2023;41:421–33.

2. López-Soto A, Gonzalez S, Smyth MJ, Galluzzi L. Control of metastasis by NK cells. Cancer Cell 2017;32:135–54.

3. Pan D, Kobayashi A, Jiang P, Ferrari de Andrade L, Tay RE, Luoma AM, et al. A major chromatin regulator determines resistance of tumor cells to T cell-mediated killing. Science 2018;359:770–5.
4. Wu L, Jin Y, Zhao X, Tang K, Zhao Y, Tong L, et al. Tumor aerobic glycolysis confers immune evasion through modulating sensitivity to T cell-mediated bystander killing via TNF-α. Cell Metab 2023;35:1580–96.e9.
5. Sheffer M, Lowry E, Beelen N, Borah M, Amara SN, Mader CC, et al. Genome-scale screens identify factors regulating tumor cell responses to natural killer cells. Nat Genet 2021;53:1196–206.
6. Freeman AJ, Vervoort SJ, Ramsbottom KM, Kelly MJ, Michie J, Pijpers L, et al. Natural killer cells suppress T cell-associated tumor immune evasion. Cell Rep 2019;28:2784–94.e5.
7. Bernareggi D, Xie Q, Prager BC, Yun J, Cruz LS, Pham TV, et al. CHMP2A regulates tumor sensitivity to natural killer cell-mediated cytotoxicity. Nat Commun 2022;13:1899.
8. Lee DH, Ahn H, Sim HI, Choi E, Choi S, Jo Y, et al. A CRISPR activation screen identifies MUC-21 as critical for resistance to NK and T cell-mediated cytotoxicity. J Exp Clin Cancer Res 2023;42:272.
9. Vredevoogd DW, Kuilman T, Ligtenberg MA, Boshuizen J, Stecker KE, de Bruijn B, et al. Augmenting immunotherapy impact by lowering tumor TNF cytotoxicity threshold. Cell 2019;178:585–99.e15.
10. Pech MF, Fong LE, Villalta JE, Chan LJ, Kharbanda S, O'Brien JJ, et al. Systematic identification of cancer cell vulnerabilities to natural killer cell-mediated immune surveillance. Elife 2019;8:e47362.
11. Kearney CJ, Vervoort SJ, Hogg SJ, Ramsbottom KM, Freeman AJ, Lalaoui N, et al. Tumor immune evasion arises through loss of TNF sensitivity. Sci Immunol 2018;3:eaar3451.
12. Patel SJ, Sanjana NE, Kishton RJ, Eidizadeh A, Vodnala SK, Cam M, et al. Identification of essential genes for cancer immunotherapy. Nature 2017;548:537–42.
13. Dufva O, Gandolfi S, Huuhtanen J, Dashevsky O, Duàn H, Saeed K, et al. Single-cell functional genomics reveals determinants of sensitivity and resistance to natural killer cells in blood cancers. Immunity 2023;56:2816–35.e13.
14. Zhuang X, Veltri DP, Long EO. Genome-wide CRISPR screen reveals cancer cell resistance to NK cells induced by NK-derived IFN-γ. Front Immunol 2019;10:2879.
15. He Y, Wang L, Wei T, Xiao YT, Sheng H, Su H, et al. FOXA1 overexpression suppresses interferon signaling and immune response in cancer. J Clin Invest 2021;131:e147025.
16. Lo HC, Xu Z, Kim IS, Pingel B, Aguirre S, Kodali S, et al. Resistance to natural killer cell immunosurveillance confers a selective advantage to polyclonal metastasis. Nat Cancer 2020;1:709–22.
17. Miyazaki S, Yamano H, Motooka D, Tashiro F, Matsuura T, Miyazaki T, et al. Zfp296 knockout enhances chromatin accessibility and induces a unique state of pluripotency in embryonic stem cells. Commun Biol 2023;6:771.
18. Gao L, Zhang Z, Zheng X, Wang F, Deng Y, Zhang Q, et al. The novel role of Zfp296 in mammalian embryonic genome activation as an H3K9me3 modulator. Int J Mol Sci 2023;24:11377.
19. Matsuura T, Miyazaki S, Miyazaki T, Tashiro F, Miyazaki J-I. Zfp296 negatively regulates H3K9 methylation in embryonic development as a component of heterochromatin. Sci Rep 2017;7:12462.
20. Poland KS, Shardy DL, Azim M, Naeem R, Krance RA, Dreyer ZE, et al. Overexpression of ZNF342 by juxtaposition with MPO promoter/enhancer in the novel translocation t(17;19)(q23;q13.32) in pediatric acute myeloid leukemia and analysis of ZNF342 expression in leukemia. Genes Chromosomes Cancer 2009;48:480–9.
21. Mizoue Y, Ikeda T, Ikegami T, Riabets O, Oishi Y, Tobita M, et al. The stem cell transcription factor ZFP296 transforms NIH3T3 cells and promotes anchorage-independent growth of cancer cells. Int J Dev Biol 2023;67:147–53.
22. Li W, Xu H, Xiao T, Cong L, Love MI, Zhang F, et al. MAGeCK enables robust identification of essential genes from genome-scale CRISPR/Cas9 knockout screens. Genome Biol 2014;15:554.
23. Pertea M, Kim D, Pertea GM, Leek JT, Salzberg SL. Transcript-level expression analysis of RNA-seq experiments with HISAT, StringTie and ballgown. Nat Protoc 2016;11:1650–67.
24. Liao Y, Smyth GK, Shi W. featureCounts: an efficient general purpose program for assigning sequence reads to genomic features. Bioinformatics 2014;30:923–30.
25. Love MI, Huber W, Anders S. Moderated estimation of fold change and dispersion for RNA-seq data with DESeq2. Genome Biol 2014;15:550.
26. Wickham H.. ggplot2: elegant graphics for data analysis. New York: Springer-Verlag; 2016.
27. Wu T, Hu E, Xu S, Chen M, Guo P, Dai Z, et al. clusterProfiler 4.0: a universal enrichment tool for interpreting omics data. Innovation (Camb) 2021;2:100141.
28. Zhang Y, Liu T, Meyer CA, Eeckhoute J, Johnson DS, Bernstein BE, et al. Model-based analysis of ChIP-Seq (MACS). Genome Biol 2008;9:R137.
29. Ramírez F, Ryan DP, Grüning B, Bhardwaj V, Kilpert F, Richter AS, et al. deepTools2: a next generation web server for deep-sequencing data analysis. Nucleic Acids Res 2016;44:W160–5.
30. Ross-Innes CS, Stark R, Teschendorff AE, Holmes KA, Ali HR, Dunning MJ, et al. Differential oestrogen receptor binding is associated with clinical outcome in breast cancer. Nature 2012;481:389–93.
31. Yu G, Wang L-G, He Q-Y. ChIPseeker: an R/Bioconductor package for ChIP peak annotation, comparison and visualization. Bioinformatics 2015;31:2382–3.
32. Wu SZ, Al-Eryani G, Roden DL, Junankar S, Harvey K, Andersson A, et al. A single-cell and spatially resolved atlas of human breast cancers. Nat Genet 2021;53:1334–47.
33. Langmead B, Salzberg SL. Fast gapped-read alignment with bowtie 2. Nat Methods 2012;9:357–9.
34. Li J, Hu H, Lian H, Yang S, Liu M, He J, et al. NK-92MI cells engineered with Anti-claudin-6 chimeric antigen receptors in immunotherapy for ovarian cancer. Int J Biol Sci 2024;20:1578–601.
35. Tam YK, Maki G, Miyagawa B, Hennemann B, Tonn T, Klingemann HG. Characterization of genetically altered, interleukin 2-independent natural killer cell lines suitable for adoptive cellular immunotherapy. Hum Gene Ther 1999;10:1359–73.
36. Hu J, Sánchez-Rivera FJ, Wang Z, Johnson GN, Ho YJ, Ganesh K, et al. STING inhibits the reactivation of dormant metastasis in lung adenocarcinoma. Nature 2023;616:806–13.
37. Diefenbach A, Jensen ER, Jamieson AM, Raulet DH. Rae1 and H60 ligands of the NKG2D receptor stimulate tumour immunity. Nature 2001;413:165–71.
38. Dong L, Chen C, Zhang Y, Guo P, Wang Z, Li J, et al. The loss of RNA N(6)-adenosine methyltransferase Mettl14 in tumor-associated macrophages promotes CD8(+) T cell dysfunction and tumor growth. Cancer Cell 2021;39:945–57.e10.
39. Bowling EA, Wang JH, Gong F, Wu W, Neill NJ, Kim IS, et al. Spliceosome-targeted therapies trigger an antiviral immune response in triple-negative breast cancer. Cell 2021;184:384–403.e21.
40. Dongre A, Rashidian M, Reinhardt F, Bagnato A, Keckesova Z, Ploegh HL, et al. Epithelial-to-Mesenchymal transition contributes to immunosuppression in breast carcinomas. Cancer Res 2017;77:3982–9.
41. Gu Y, Zhang Z, Camps MGM, Ossendorp F, Wijdeven RH, Ten Dijke P. Genome-wide CRISPR screens define determinants of epithelial-mesenchymal transition mediated immune evasion by pancreatic cancer cells. Sci Adv 2023;9:eadf9915.
42. Kloet SL, Karemaker ID, van Voorthuijsen L, Lindeboom RGH, Baltissen MP, Edupuganti RR, et al. NuRD-interacting protein ZFP296 regulates genome-wide NuRD localization and differentiation of mouse embryonic stem cells. Nat Commun 2018;9:4588.
43. Reid XJ, Low JKK, Mackay JP. A NuRD for all seasons. Trends Biochem Sci 2023;48:11–25.
44. Hu G, Wade PA. NuRD and pluripotency: a complex balancing act. Cell Stem Cell 2012;10:497–503.
45. Liu Y, Peng Y, Du W, Yu C, Peng Z, Qin L, et al. PD-L1-mediated immune evasion in triple-negative breast cancer is linked to the loss of ZNF652. Cell Rep 2023;42:113343.
46. Deng P, Wang Z, Chen J, Liu S, Yao X, Liu S, et al. RAD21 amplification epigenetically suppresses interferon signaling to promote immune evasion in ovarian cancer. J Clin Invest 2022;132:e159628.